ELSEVIER

Journal of Nuclear Materials 278 (2000) 277–289

journal of nuclear materials

www.elsevier.nl/locate/jnucmat

The corrosion of materials in water irradiated by 800 MeV protons

R.S. Lillard *, D.L. Pile [1], D.P. Butt [2]

Materials Corrosion and Environmental Effects Laboratory, Materials Science and Technology Division, Materials Technology: Metallurgy MST-6, P.O. Box 1663, MS G775, Los Alamos National Laboratory, Los Alamos, NM 87545, USA

Received 11 June 1999; accepted 15 September 1999

Abstract

A method for measuring the real-time corrosion rates for Alloy 718, stainless steels (SS) 304L and 316L nuclear grade (NG), aluminum alloys 5052 (Al5052) and 6061 (Al6061), copper (Cu), tantalum (Ta), and tungsten (W) in two separate water systems that were irradiated by 800 MeV protons is presented. The first water system was fabricated entirely of 304 SS, thoroughly cleaned before operation, and employed hydrogen water chemistry (HWC) to mitigate the formation of some of the radiolysis products. The samples were adequately shielded from the irradiation cavity such that only the effects of water chemistry were investigated. Over the course of that irradiation period the corrosion rates for 304L SS, 316L-NG SS, Alloy 718, and Ta were less than 0.12 μm/yr. For Al6061 and Al5052, the corrosion rates were of the order of 0.50–2.0 μm/yr. The corrosion rate of W was relatively high between 5.0 and 30 μm/yr. The second water system, fabricated from copper piping and steel components, was not cleaned prior to operation, and employed no HWC. In comparison to the other system, the corrosion rates in the copper/steel system were 1–3 orders of magnitude higher. These results are discussed in terms of water radiolysis and water impurity levels.

1. Background

1.1. Water radiolysis

Spallation neutron sources typically consist of a high energy (0.6–1.4 GeV) proton accelerator (linac/synchrotron) and a shielded cavity which contains the neutron source (or target). This target is a high atomic number metal, for example tungsten (W) or tantalum (Ta). High-energy neutrons are produced when the proton beam leaves the high vacuum of the accelerator via a 'window' and enters the cavity where it then strikes the target. To keep the target cool (and to moderate the energy of the neutrons which are produced) it is enclosed in a cooling loop which is generally constructed from stainless steel 304 (304 SS) and filled with deionized water. The interaction of high-energy protons with water results in the breakdown of water molecules to form a myriad of stable and short-lived species. Water radiolysis models for both fission reactors [1–3] and linear accelerators [4] predict that similar species are formed in both environments including: H_2, O_2, H_2O_2, OH, H, e^-_{aq}, HO_2, O_2^-, HO_2^-, OH^-, H^+. A list of some of the possible decomposition mechanisms for these species and their respective rate constants are presented in Table 1. As indicated by the reaction rate constants, the lifetime of many of these species is short, of the order of microseconds to nanoseconds. The steady-state concentration of these short-lived species is typically of the order of 10^{-7}–10^{-5} mol/m^3. Therefore, while these short-lived species may be an important consideration in the corrosion mechanism at the proton beam/metal/solution interface, where the steady-state concentration will be

* Corresponding author. Tel.: +1-505 667 6325; fax: +1-505 667 8021.

E-mail address: lillard@lanl.gov (R.S. Lillard).

[1] Present address: Department of Materials Science, University of Virginia, Charlottesville, VA 22903, USA.

[2] Present address: Ceramatec Inc., 2425 South 900 West, Salt Lake City, UT 84119, USA.

0022-3115/00/$ - see front matter
PII: S0022-3115(99)00248-2

Table 1
Elementary equations showing some of the water radiolysis products formed during irradiation, their decomposition mechanism, rate constant, and activation energy (from Ref. [5])

Reaction	Rate constant $(s)^{-1}$	Activation energy (J/mol)
$e^- + H_2O = H + OH^-$	2.4×10^{10}	1.26×10^4
$e^- + OH = OH^-$	3.0×10^{10}	1.26×10^4
$H + H = H_2$	1×10^{10}	1.26×10^4
$e^- + HO_2 = HO_2^-$	2×10^{10}	1.26×10^4
$OH + OH = H_2O_2$	**4.5×10^9**	**1.26×10^4**
$H + OH = H_2O$	**2.4×10^{10}**	**1.26×10^4**
$H + O_2 = HO_2$	1×10^9	1.26×10^4
$OH^- + H_2O_2 = HO_2^- + H_2O$	1×10^8	1.89×10^4
$HO_2 = O_2^- + H^+$	8×10^5	1.26×10^4

high while the beam is on, they will have little impact on materials 'downstream' in the cooling water loop.

Radiolysis products such as hydrogen peroxide (H_2O_2), oxygen (O_2), and hydrogen (H) are the species most likely to influence the corrosion reaction mechanism of materials downstream from the beam because their lifetimes are of the order of days or weeks and, they are oxidizing species [5]. At the open circuit potential (OCP), anodic and cathodic reactions on the metal surface occur at the same rate. As corrosion reactions are generally cathodically limited, an increase in the concentration of an oxidizing species increases the cathodic reaction rate and, correspondingly, increases the anodic (metal oxidation) reaction [6]. It has been shown that an increase in concentration of total oxidant due to water radiolysis results in an increase in the OCP of structural materials in the cooling loop, such as austenitic stainless steels, to a potential region which is associated with an increased risk for stress corrosion cracking (SCC). Therefore, it is anticipated that the unmitigated production of H_2O_2 in a spallation neutron cooling water loop will result in higher corrosion rates as compared to a system that attempts to control the concentration of total oxidant ($H_2O_2 + O_2$) by the addition of a scavenger gas (such as H_2) [5]. For example, H_2O_2 is formed when two OH radicals combine:

$$OH + OH \xrightarrow{k_1} H_2O_2, \quad k_1 = 4.5\times10^9\ s^{-1}. \tag{1}$$

By bubbling H_2 gas into the system, the OH radical preferentially reacts with the resultant dissolved atomic hydrogen in the cooling loop to form water:

$$OH + H \xrightarrow{k_2} H_2O, \quad k_2 = 2.4\times10^{10}\ s^{-1}. \tag{2}$$

A similar reaction sequence can be written for O_2 formation and suppression. The ability of H_2 to suppress the concentration of total oxidant in a water system exposed to radiation has long been recognized by the boiling water reactor (BWR) community and is referred to as hydrogen water chemistry (HWC). To mitigate the increased susceptibility to SCC that results from high concentrations of total oxidant, a typical BWR operates at a dissolved hydrogen concentration of the order of 0.05 mol/m^3. For BWRs as well as pressurized water reactors, the OCP is greatly suppressed during HWC [7–13]. The OCP can further be reduced by plating a small film (tens of nm thick) of noble metal onto the interior surface of these components [14]. These noble metals (such as Pd or Pt) have a high exchange current density for the reversible hydrogen reaction and, in combination with HWC, decrease the OCP to the potential for the reversible hydrogen reaction which is below the threshold potential for SCC.

1.2. Corrosion in irradiated water

Investigations of the effects of radiolyzed water on corrosion rate can be divided into two general categories: (1) simulated environments and (2) experiments where the electrochemical cell containing the working electrode (or weight loss coupon) is placed in either a Co^{60} or Ce^{137} source. In this latter category of experiments, the OCP of stainless steels [15] and titanium [16] has been observed to shift in the noble direction during irradiation. This positive increase in the OCP has been attributed to the radiolytic production of hydrogen peroxide, in a mechanism similar to that described above. However, by the nature of their set-up these experiments expose both the water and sample to γ-radiation and, therefore, do not separate the effect of radiolysis products from those effects associated with the direct γ-radiation of the sample. The direct exposure of metals to irradiation has been shown to affect both the defect structure and the conducting properties of the passive oxide, thus affecting metal dissolution rate and susceptibility to pitting [17,18]. For example, potentiodynamic polarization curves for Ti after 12 months exposure to brine solution with γ-radiation show small decreases in anodic current densities and limited thickening of the passive film as compared to unirradiated samples [19]. X-ray photoelectron spectroscopy of the

passive film on stainless steel after exposure to γ-radiation found that the surface oxide was depleted in iron and enriched in chromium [20]. Therefore, to investigate the effects of long-lived water radiolysis products on corrosion rate, any effects due to sample radiation should be eliminated.

1.3. Present investigation

The purpose of this investigation is to study changes in water quality during 800 MeV proton irradiation and characterize the effect of these changes on the corrosion rates of metals. The effects of direct sample radiation on corrosion rate were minimized by separating the water manifold, that allowed water to be circulated through the proton beam, from the corrosion probes with adequate distance and shielding. We hope to demonstrate that the corrosion rates of materials in a spallation neutron cooling loop can be minimized by a combination of pre-operation cleaning of the water system, hydrogen water chemistry to reduce peroxide formation, deionized cooling water, and on-line filters.

2. Experimental

2.1. The water systems

This paper reports the results from corrosion samples studied in two separate water systems. These systems shall be referred to as the 'corrosion loop' and the 'degrader loop' (Fig. 1(a) and (b), respectively). Both systems were irradiated at the Los Alamos Neutron Science Center (LANSCE) A6 Target Station. Diagrams of this area may be found in earlier publications [21]. The degrader loop was in operation during the late summer and early fall of 1995 while the corrosion loop was in operation during the spring and early summer of 1997. Each loop was attached to a water manifold that was directly exposed to 800 MeV protons during the course of the experiments. In the case of the degrader loop, the manifold consisted of a football-shaped water baffle. Water flowing through this baffle had a residence time of approximately 16 s. In the case of the corrosion-loop, the water manifold held a set of the in-beam corrosion probes. Results from these in-beam probes, which examined the effects of proton irradiation on corrosion rate, have been discussed in separate publications [22,23].

The corrosion loop (Fig. 1(a)) was a closed loop system and constructed entirely of 304 SS. [3] While most of the connections to this system were welded, threaded connections were sealed with nuclear reactor grade pipe dope. The nominal operating pressure was 1.03×10^6 Pa at a flow rate of 1 liter/s. and a temperature of 20°C. Prior to placing the corrosion loop into operation it was steam cleaned. This was followed by several rinsings with a 50% DI water/50% ethanol mixture. Finally, the system was rinsed several times with DI water. Each rinse consisted of filling the expansion and reservoir tanks with the solution and circulating it through the system with the pump. In an attempt to mitigate the formation of hydrogen peroxide in the corrosion loop, HWC was employed. This was accomplished by bubbling a mixture of H_2/94% Ar gas directly into the water reservoir. The dissolved hydrogen concentration in the corrosion loop during the LANSCE irradiation experiments was monitored with a remote hydrogen sensor, Orbisphere Laboratories, Emerson NJ (model #3610/220.E, TCD Hydrogen Gas System). Nominally, the system was operated with a dissolved hydrogen concentration of approximately 0.40 mol/m^3. During some periods of irradiation the measured hydrogen concentration was greater than this value, presumably due to radiolytic hydrogen formation.

The degrader loop was also a closed loop (Fig. 1(b)). Although the water baffle and piping associated with the insert were constructed entirely of 304 SS, the piping associated with the pumping system and heat exchanger was constructed from copper as well as steel. Unlike the corrosion loop, no special cleaning of the system was employed before operation. Although the system was filled with deionized water, no HWC was employed. Nominally, the degrader loop operated at a pressure of 6.2×10^5 Pa, a flow rate of 0.32 l/s, and a temperature of approximately 30°C.

Both the corrosion and degrader water loops contained identical probes for measuring corrosion rate. These probes were located out-of-beam, downstream from the manifold and a considerable distance from any proton/neutron flux (designated as return and supply corrosion probes in Fig. 1(a) and (b)). They were purchased off-the-shelf from a commercial vender. A diagram of the probe can be found in earlier publications [21]. The probe consisted of a 304 SS national pipe thread (NPT) pipe plug style feed-through that supported three threaded studs. These studs were joined to the NPT feed-through via a glass to metal seal that also provided electrical isolation. One end of the sample was tapped to accept the threaded stud on the feed-through. Electrical contact to the sample was made via a coaxial cable and BNC connector on the feed-through. A water tight seal between the sample and glass was obtained via a Viton o-ring that was placed on each stud prior to screwing on the samples. The probes were fitted into 'cells' constructed from 304 SS on both the supply and return sides of the cooling water loop at the top of the insert (approximately 3.4 m from the proton beam).

[3] It is recognized that stainless steel 308 welded rods are used in the welding of 304 SS.

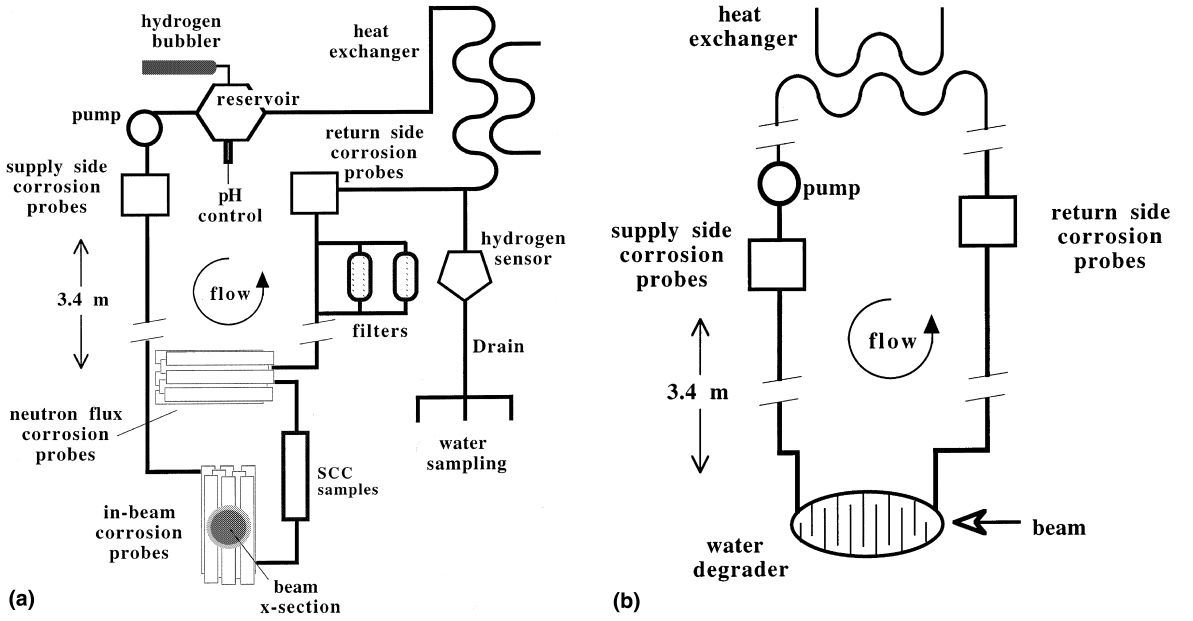

Fig. 1. (a) Diagram representing the corrosion loop. The 800 MeV proton beam struck the water loop at the base of the insert (in-beam corrosion probes). The radiolyzed water then circulated from the beam spot through the remainder of the loop including the out-of-beam probes. (b) Diagram representing the degrader loop. Water circulated through the degrader where it was irradiated by 800 MeV protons. The radiolyzed water then circulated from the beam spot through the remainder of the loop including the out-of-beam probes.

These cells contained an inlet and outlet for the system water and held approximately 8 liters of water. A modified version of the three electrode out-of-beam corrosion probes was used to measure changes in water conductivity in both the corrosion and degrader loop. In the corrosion loop, the conductivity probes were constructed by welding a hollow 304 SS sleeve (approximately 7.5 cm long, 4 cm ID, and 0.15 cm wall) onto two of the threaded sample mounting studs of the NPT feed-through. This stainless steel sleeve surrounded a small 304 SS rod (6.4 cm long, 0.03 cm diameter) which was welded onto the third sample mounting stud. Because both ends of the sleeve were open and there was a separation distance of approximately 0.5 cm between the sleeve and the NPT feed-through, ample water flowed from one end of the sleeve to the other. To determine the cell constants of these probes, each probe was calibrated with solutions of known conductivity prior to placement in the system. One conductivity probe was placed in the supply stream and one in the return stream cells at the top of the inserts. Similar probes were used to measure conductivity in the degrader loop.

2.2. Proton beam characteristics

The proton beam characteristics at LANSCE have been described in detail elsewhere [23,24]. Briefly, the proton beam flux at the LANSCE A6 Target Station had a Gaussian distribution of $2\sigma \approx 3$ cm. The energy of this particle beam was 800 MeV. The beam had a characteristic macropulse repetition rate of 100 Hz, a gate length of 835 μs, and a fixed peak current of 16 mA. Average proton beam currents were controlled by varying the spacing between each micropulse (and therefore the number of micropulses) in the gate. Nominally, the average proton-beam currents varied between 0.001 and 1.0 mA. Calculated proton fluence at the manifold of the corrosion loop as a function of irradiation time is presented in Fig. 2 [23]. The measured

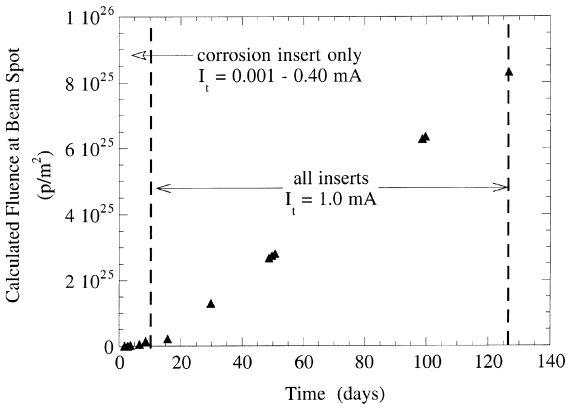

Fig. 2. Calculated proton fluence at the corrosion loop manifold as a function of irradiation time (in accordance with Ref. [23]). I_t represents the proton beam current.

fluence on both the degrader and corrosion manifolds at the end of the irradiation periods was of the order of 10^{25} p/m^2. Although all experiments were conducted with the proton beam on (unless otherwise noted in the text), it should be re-emphasized that the out-of-beam samples reported on here were both up stream and down stream from the manifolds, well shielded from the proton beam and any secondary radiation.

2.3. Electrochemical

Corrosion samples were fabricated from rods approximately 0.318 cm in diameter by 5–7.6 cm in length. The samples placed in the corrosion loop were: Alloy 718 (UNS N07718, precipitation hardened), aluminum alloys 6061 (UNS A96061, T6 temper, referred to as Al6061) and 5052 (UNS A95052, T6 temper, referred to as Al5052), 304L SS (UNS S30403), 316L stainless steel nuclear grade (UNS S31653, referred to as 316L-NG SS), 99.8% tungsten (W), and 99.95% tantalum (Ta). The samples placed in the degrader loop were Al6061, 304L SS, Alloy 718, and 99.99% copper (Cu). Prior to placing the corrosion samples on the probe, the surfaces were abraded with 600 grit SiC paper to expose a fresh metal/oxide surface for electrochemical characterization. The samples were then cleaned in an ultrasonic cleaner in successive baths of acetone, ethanol and DI water. The reference electrode was made by flame-oxidizing (in air) a tungsten sample [25]. This reference electrode is referred to here as W/Wox. The pH of the water in the corrosion loop was measured during operation and found to be approximately 4.2. The OCP of the W/Wox reference electrode at pH 4.2 was −0.045 V relative to saturated calomel ($OCP_{W/Wox} = 0.08–0.03$ pH; V vs. SCE). Therefore, the corrosion loop sample potentials measured with the W/Wox electrode were normalized to the SCE scale by subtracting −0.045 V. In addition, because the OCP of W/Wox electrode changed only 0.03 V/pH unit, corrections for small deviations in the water system pH were not needed. Further, the OCP of the W/Wox electrode was independent of hydrogen concentration as shown in Fig. 3. Upon adding 0.1 M H_2O_2, the potential of the W/Wox electrode increased by approximately 0.17 V. Therefore, for small increases in peroxide concentration (ppm) we shall assume the change in potential of this electrode from its steady-state value is negligible.

To measure the polarization resistance (R_{pol}) of each sample as a function of irradiation conditions, electrochemical impedance spectroscopy (EIS) was used. EIS is a powerful non-destructive technique for measuring the corrosion rates of metals in aqueous environments [26,27] and is ideally suited for systems with high solution resistivity such as in DI water. Here a small sinusoidal voltage perturbation (30 mV) was applied across the sample interface over the frequency range of

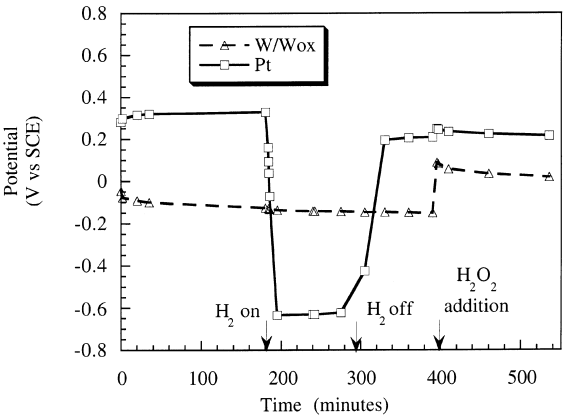

Fig. 3. OCP of the tungsten/tungsten-oxide and platinum electrodes (vs. saturated calomel electrode SCE) as a function of time. Plot shows the effect of bubbling H_2 gas into solution and the addition of 0.1 M H_2O_2 on the OCP of these electrodes.

0.003–1.0 kHz. By measuring the transfer function of the applied ac voltage perturbation and the ac current response of the sample, an impedance resulted ($Z_\omega = V_\omega/I_\omega$). In the simplest sense, at low frequencies the sample behaved as a resistor and the impedance was equal to the sum of the polarization and solution resistance ($Z_{lo} = (R_{sol} + R_{pol})$). At high frequencies, the sample behaved as a capacitor and, therefore, offered no resistance to the ac current and $Z_{hi} = R_{sol}$. By measuring Z_ω over a wide frequency range, R_{pol} can be quantified by subtracting Z_{hi} from Z_{lo}. All EIS experiments were conducted at the sample's OCP (i.e., its free corrosion potential). Data were collected in the traditional three electrode configuration where the W/Wox electrode served as a reference and three, electrically connected, alloy C276 samples served as the counter electrode. In addition, the EIS system used in this investigation operated with a floating ground to avoid interference from ground loops.

For the corrosion loop, initial irradiation experiments were conducted during proton irradiation at average proton beam currents of 0.001, 0.010, 0.04, 0.10, and 0.40 mA and while the proton beam was on. These data were taken with all other inserts (17A–18C in Fig. 4) pulled out of the proton beam path such that the first material that the proton beam struck after leaving high vacuum was tube no. 1 of the corrosion manifold (17B). Thermocouples attached to the front of the manifold verified the position, size and shape of the proton beam. After approximately 300 h of experiments with only the corrosion insert in place, inserts 17A, 18A, 18B, and 18C were placed in position in front of the corrosion insert and the beam current was increased to 1.0 mA. The effect of these inserts in front of the corrosion insert was to spread the proton beam from its compact Gaussian distribution to a more diffuse, cloud-like beam. That is,

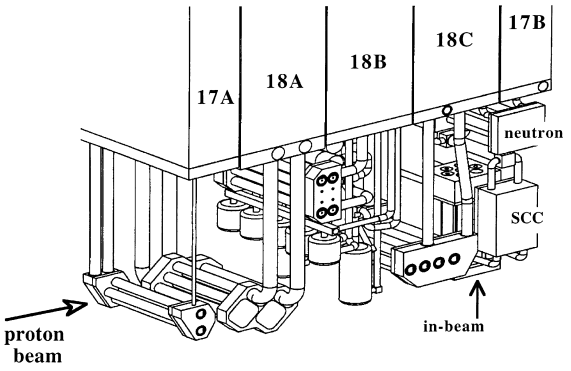

Fig. 4. A diagram representing the A6 Target Station at LANSCE and placement of the corrosion loop (17B). Early in-beam data reported on for the corrosion loop were collected with inserts 17A–18C removed from the beam path. At later times, inserts 17A–18C were placed in-beam as shown in this figure.

for any given current the beam flux at the corrosion loop insert was lower with the forward inserts in place.

For the degrader loop, all experiments were conducted at a beam current of 1 mA. Unlike the corrosion loop, at no time were inserts placed between the ultra-high vacuum window and the water degrader manifold. Therefore, there is no reason to expect that the beam flux deviated from the anticipated profile [24] during the course of the experiments.

3. Results and discussion

3.1. OCP measurements

For the materials that were the most active (least noble), some difference was observed between the OCP of the return side sample and the OCP of the supply side sample during irradiation. This is best illustrated in the OCP of the Cu samples in the degrader loop (Fig. 5). When the beam was turned on, a sharp 0.075 V increase in the OCP of the return side sample from its steady-state value was observed. In addition, when the beam was shut off, a sharp decrease in the OCP was also observed. No change in the OCP of the supply side probe from its steady-state value was observed when the beam was turned on. In addition to the changes observed in the OCP of the return side samples, a gradual increase in the OCP of all samples (supply and return, degrader and corrosion loops) was observed over the course of both irradiation periods (Fig. 6). This gradual increase in OCP with irradiation time is consistent with an increase in the concentration of total oxidant as discussed above.

Steady-state H_2O_2 formation in the corrosion loop was measured by iodometric titration of water samples

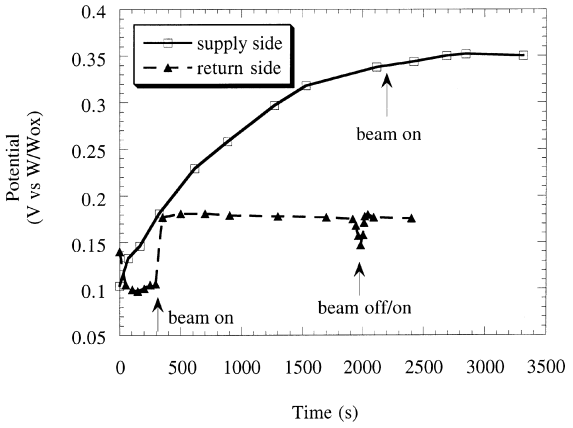

Fig. 5. OCP of the return and supply side Cu samples in the degrader loop. Although plotted on the same graph, the return and supply experiments were conducted at different times, that is, 'beam on' during the return side experiments does not correlated with beam on in the supply side experiment.

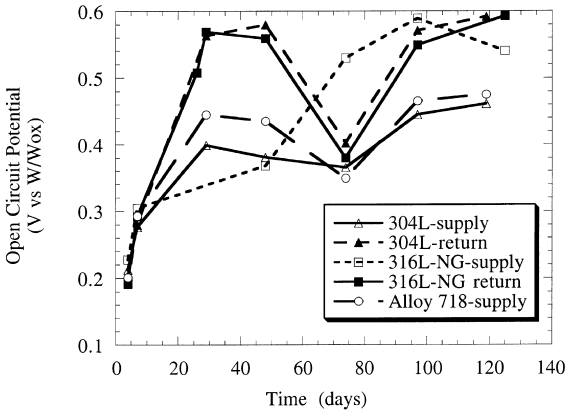

Fig. 6. OCP of 304L SS, 316L-NG SS, and Alloy 718 samples in the corrosion water loop for both the supply side, and return side as a function of irradiation time.

taken from the system (a technique sometimes called Kingzettís method). Briefly, a volume of irradiated water was placed in a conical flask. Enough sulfuric acid was added to the water to adjust the pH to 1 (approximately). An excess amount of iodide ions, I^-, is added to this solution, thereby producing triiodide ions:

$$H_2O_2 + 3I^- \rightarrow I_3^- + 2H_2O. \quad (3)$$

The reaction is quantitative: each hydrogen peroxide molecule reacts and produces exactly one triiodide ion; the excess iodide ions remain in solution and do not interfere with the rest of the analysis. The triiodide ions that were produced were then titrated with a standardized solution of sodium thiosulfate. While no H_2O_2 was

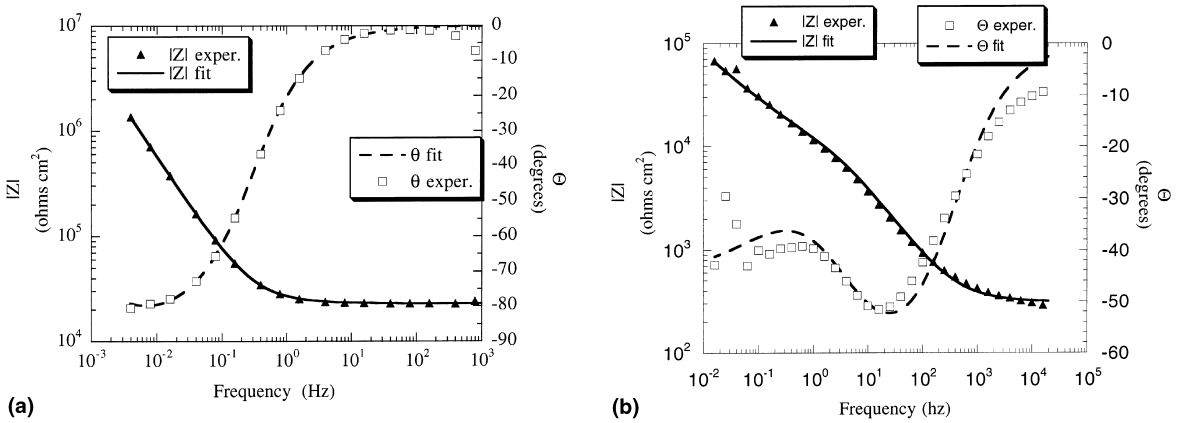

Fig. 7. Bode magnitude $|Z|$ and phase (θ) plots for the out-of-beam samples: (a) alloy 718 sample (supply side, corrosion loop); and (b) 304L SS sample (return side, water degrader loop). Not all experimental data (□/▲) are presented. Solid and dashed lines represent complex non-linear least square fits to the data.

detected in the corrosion loop during the first 20 days of irradiation, the H_2O_2 concentration gradually increased to a final value of 0.34 mol/m^3. This value was quite low in comparison to the amount of H_2O_2 the system was theoretically capable of producing [4]. As Eqs. (1) and (2) above are competing reactions, some amount of H_2O_2 production is anticipated. Specifically, the ratio of the rate of H_2O formation relative to H_2O_2 formation is 4.6[H]/[OH]. Therefore, increasing the concentration of dissolved H should decrease the H_2O_2 concentration further. It may also be noted that H_2O_2 formation may be self limiting as water radiolysis also produces a substantial amount of H. That is, in the absence of HWC, a sufficient concentration of H may be produced by radiolysis such that the actual H_2O_2 concentration will be below the theoretical value.

3.2. CNLS modeling of EIS data and corrosion rate

Typical EIS data are presented in Fig. 7(a) for Alloy 718 (corrosion loop) and Fig. 7(b) for 304L SS (degrader loop). These figures are representative of the data for all samples in this study although the magnitude of the impedance was a function of sample material, sample location, and beam parameters. The equivalent circuits (EC) used to model these data are presented in Fig. 8. The EC in Fig. 8(a) is referred to as a simplified Randle's circuit and was used when the response of the material was similar to that in Fig. 7(a). In this model, R_{pol} represents the polarization resistance of the material, C_{dl} the double layer capacitance, and R_{sol} the geometric solution resistance between the working and reference electrodes. Typical curve fits of this model to the data are presented in Fig. 7(a) as solid and dashed lines. As can be seen in this figure, good agreement between the model and the data exists. At longer immersion times a Warburg (diffusion) component in the EIS spectra of some samples was observed. The diffusion impedance was characterized by a change in the slope of the plot of $|Z|$ vs. frequency from -1 to approximately $-1/2$ at approximately 4.0 Hz (Fig. 7(b)). For these data, the EC in Fig. 8(b) was used, where Z_W represents the diffusional (Warburg type impedance) and all other elements are as before. Once again, good agreement between the model and the experimental data exist as represented by the solid and dashed lines in Fig. 7(b).

From the CNLS values of R_{pol}, the corrosion rate of each sample was calculated as a function of immersion time. In these calculations, i_{corr} was derived from R_{pol} by the Stern–Geary relationship [28]

$$R_{pol} = \Delta E/\Delta i_{app} = \frac{\beta_a \beta_c}{2.3 i_{corr}(\beta_a + \beta_c)}, \quad (4)$$

where Δi_{app} is the change in applied current density, i_{corr} the corrosion current density, ΔE is equal to the difference between E_{corr} (the OCP) and E_{app} (the applied potential), [4] and β_a and β_c are the anodic and cathodic Tafel slopes. Because the anodic and cathodic Tafel slopes for these materials in radiolyzed DI water were not known (and not easily determined) they were assumed to be 0.12 V/decade current. It may be noted that typical minimum and maximum values for β_a and β_c differ only by a factor of 3 (0.06 and 0.18 V respectively), therefore, i_{corr} is more sensitive to changes in R_{pol} as compared to changes in β_a and β_c [29]. From i_{corr}, the corrosion rate (CR, in μm/yr) was determined from the well-known relationship

[4] Here, E_{app} is equal to the potential of the ac perturbation and i_{app} the response of the sample to that perturbation.

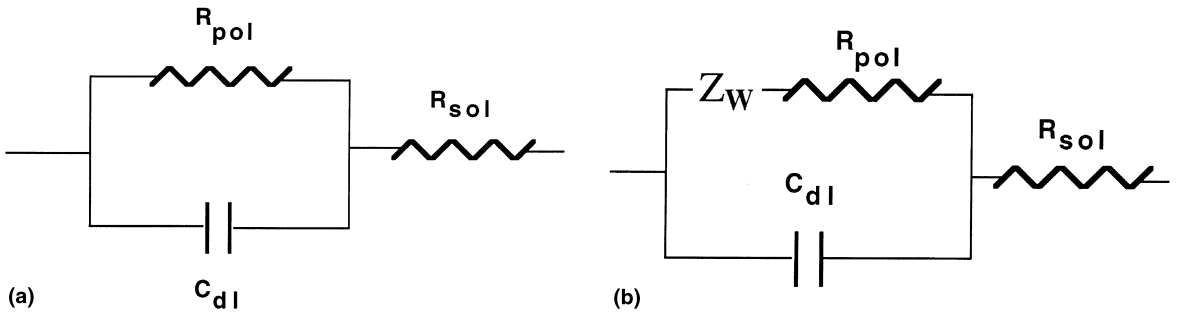

Fig. 8. Electrical equivalent circuits used to model EIS data: (a) simplified Randle's circuit and (b) diffusion impedance circuit.

$$\mathrm{CR} = \frac{3.27 \times 10^5 \left(0.026/R_{\mathrm{pol}}\right)(\mathrm{EW})}{\rho}, \tag{5}$$

where ρ is the density in kg/m^3, the units conversion constant 3.27×10^5 has units of (kg/μm)/(m/mA/yr), and EW is the equivalent weight of the material and is dimensionless. Caution is warranted, however, when using Eq. (5) to calculate corrosion rates. As i_{corr} is the corrosion current density, it has been normalized by the total surface area of the sample. Therefore, Eq. (5) yields a surface averaged rate and may not be conservative if pitting type corrosion has occurred. That is, in pitting corrosion the majority of the corrosion current is associated with a very small area on the surface of the sample.

3.3. Corrosion rates in the corrosion loop

Corrosion rates for W and 316L-NG SS are presented in Figs. 9 and 10 as a function of immersion time. The irradiation period has been divided into three separate categories in these plots: (1) pre-irradiation, beam off (indicated by negative days), (2) beam on 0.001–0.40 mA, corrosion insert only (days 0–10), and (3) beam on 1 mA, all forward inserts in place (after day 10). During experiments when only the corrosion insert was in-beam, the beam spot at the corrosion manifold had a Gaussian distribution of $2\sigma = 3$ cm. After day 10, the forward inserts were placed in-beam. This resulted in a decrease in proton flux for any given proton beam current at the corrosion manifold after day 10. As shown in Figs. 9 and 10 the corrosion rate of these samples was greatest during the first 10 days of the irradiation period when only the corrosion insert was in place. More importantly, it appears that corrosion rate increased with beam current during this period, the greatest increase being observed in the return side probe. This can be seen more clearly in Fig. 11. With only the corrosion loop in place, the corrosion rate of the return side W sample increased from 2.19 μm/yr with the beam off to 32.7 μm/yr at a beam current of 0.40 mA. In comparison, the change in corrosion rate of the supply side probe appears to be less dependent on beam current.

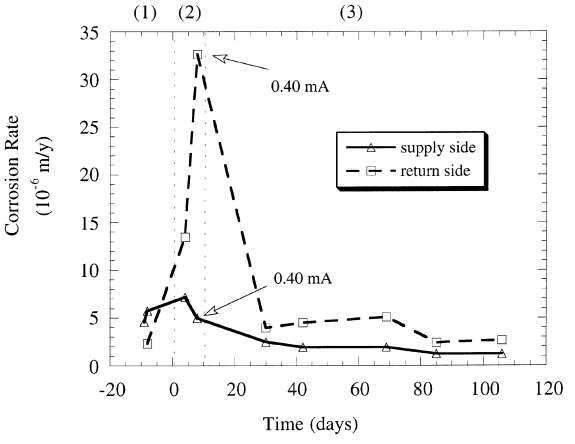

Fig. 9. Corrosion rates for W in the corrosion water loop as a function of irradiation time. The irradiation period has been divided into three separate categories: (1) pre-irradiation, beam off; (2) beam on, 0.001–0.40 mA, corrosion insert only; and (3) beam on, 1 mA, inserts 17A–18C in place.

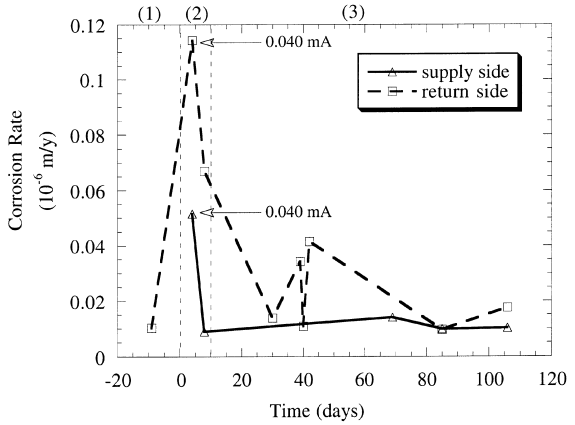

Fig. 10. Corrosion rates for 316L-NG SS in the corrosion water loop as a function of irradiation time. The irradiation period has been divided into three separate categories as described in Figs. 2 and 9.

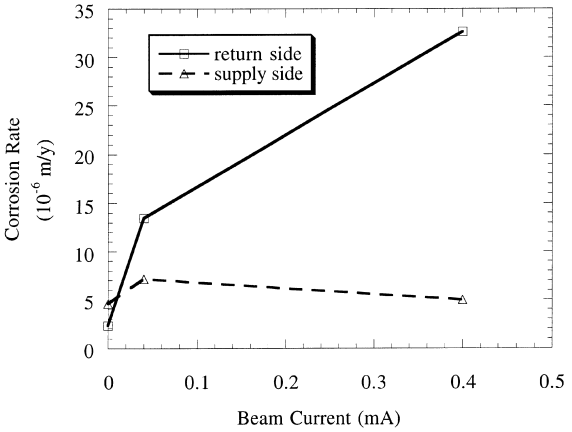

Fig. 11. Corrosion rates for W in the corrosion loop as a function of beam current. Data taken during days 0–10, corrosion insert only (Part 2 in Fig. 9).

The observed changes in W corrosion rate appear to be independent of water resistivity (Fig. 12). After several flush and refills of the corrosion water system during the pre-irradiation period, initial water resistivity rose to approximately 7.8×10^4 Ω cm prior to irradiation. The low resistivity in the first several days before the beam was turned on likely owed to impurities that were being washed from the walls of the water system. After turning the proton beam on, a sharp decrease in the water resistivity from 7.8×10^4 to 4.1×10^4 Ω cm was observed. This may be due to a combination of water radiolysis products and radiolysis enhanced cleaning of the system. When the corrosion rate of W in this time period (Fig. 11) is compared with the observed changes in water resistivity, no apparent correlation between corrosion rate and water resistivity is seen. One would anticipate that corrosion rate would be inversely proportional to water resistivity.

Changes in the corrosion rate of Al6061, and Al5052 (corrosion loop, Figs. 13 and 14, respectively) appear to be similar for the return and supply side probes and independent of beam current or irradiation time. A small 'peak' in corrosion rate around day 40 was observed in 3 of the 4 aluminum samples. This peak corresponds to a minimum in the water resistivity on day 40. After day 40 a small (unrepairable) leak in the water system (approximately 1 liter/h) required fresh DI to be pumped into the system to maintain operating condi-

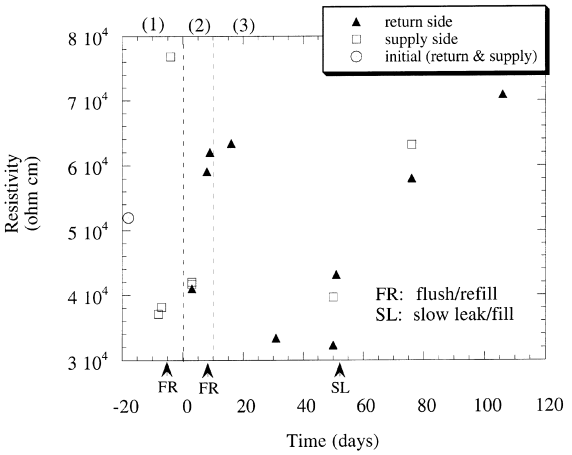

Fig. 12. Water resistivity from the corrosion loop as a function of irradiation time as measured by the supply and return probes. The irradiation period has been divided into three separate categories as presented in Figs. 2 and 9.

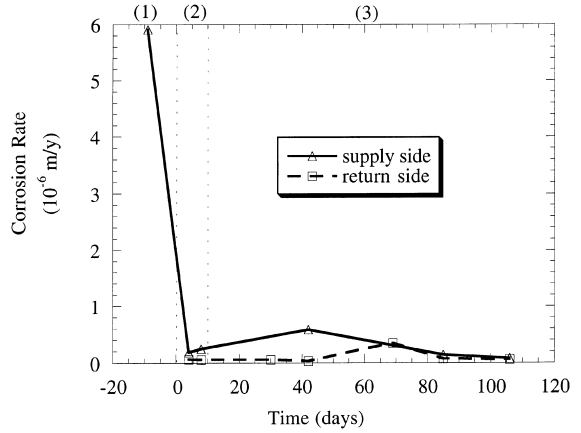

Fig. 13. Corrosion rates for Al6061 in the corrosion water loop as a function of irradiation time. The irradiation period has been divided into three separate categories as described in Figs. 2 and 9.

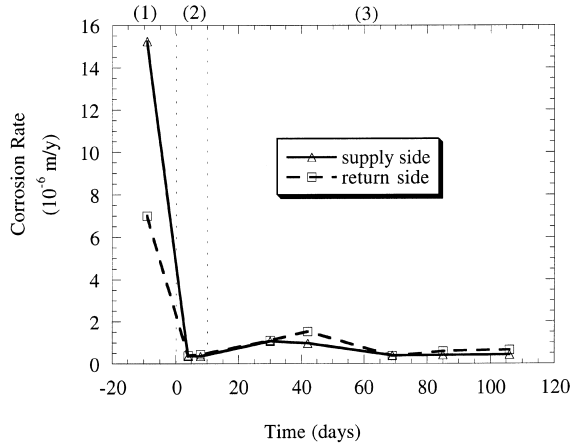

Fig. 14. Corrosion rates for Al5052 in the corrosion water loop as a function of irradiation time. The irradiation period has been divided into three separate categories as described in Figs. 2 and 9.

Table 2
Gamma analysis of water samples taken from the corrosion water loop as a function of time (in dpm). The beam was turned on at day 0. The system was flushed and refilled with fresh water on day 6 and 8

Days of irradiation	Be^7	Mn^{54}	Sc^{64}	Co^{56}	Co^{60}
−11	None detected	None detected	None detected	None detected	None detected
7	2.3×10^4	100	None detected	None detected	None detected
9	8.7×10^4	400	178	None detected	None detected
66	4.0×10^6	9.2×10^3	465	7.4×10^3	840

Table 3
ICP analysis of water samples taken from the corrosion water loop as a function of time. Concentrations are in mole/m^3. Hydrogen peroxide concentration from iodometric titration is also presented. The beam was turned on at day 0. The system was flushed and refilled with fresh water on day 6 and 8

Days of irradiation	W	Mg	Zn	Cu	Ca	Fe
−11	5.4×10^{-5}	1.3×10^{-3}	6.1×10^{-4}	3.1×10^{-4}	0.0065	None detected
7	None detected	5.4×10^{-3}	6.9×10^{-3}	6.3×10^{-4}	0.0072	None detected
9	3.3×10^{-4}	2.1×10^{-3}	2.9×10^{-3}	6.3×10^{-4}	0.0047	None detected
66	3.4×10^{-3}	3.7×10^{-3}	4.6×10^{-3}	4.7×10^{-4}	0.0060	None detected
132	H_2O_2 concentration = 0.34					

tions. As anticipated, this resulted in an increase in water resistivity in the corrosion loop after day 40 (Fig. 12).

The highest corrosion rates for the aluminum alloys were observed during the pre-irradiation period. This was attributed to chloride, sulfate, and other contaminants that may not have been removed from the system during the cleaning process. Gamma analysis of water samples taken from the corrosion loop found that the water activity owing to Mn^{54}, Co^{56}, Co^{60} increased with proton irradiation time as presented in Table 2 (Be^7 is a spallation product of oxygen). These levels were relatively low, and were attributed to the relatively low corrosion rates of the 304 SS water system as well as the in-beam Alloy 718 and 304 SS corrosion samples. This was confirmed by inductively coupled plasma (ICP) measurements which found no measurable iron in the system and only trace levels of Mg, Zn, Cu, and Ca impurities. The concentration of these impurities remained relatively constant during the irradiation period (Table 3). In addition, similar concentrations of these impurities were found in the unirradiated DI water.

The corrosion rate of the 304L SS, Alloy 718, and Ta samples (corrosion loop, Figs. 15–17) were apparently immune to changes in water chemistry, beam current, or irradiation time. No trends in corrosion rate with immersion time were observed in these samples. In addition, the corrosion rates of all of these samples were less than 0.12 μm/yr. Although the Ta corrosion rates were the lowest observed (Fig. 17), the corrosion rate of the supply side Ta sample increased with time independent of the proton beam current or flushing of the water system. Therefore, this trend is likely due to a change in the probe or sample integrity such as crevicing at the Viton gasket or the failure of this gasket to adequately insulate the Ta sample from the probe assembly. Unfortunately, due to the high radiation levels, the necessary visual access to the sample to confirm this was not possible .

3.4. Corrosion rates in the degrader loop

Similar trends in corrosion rate with beam current were also observed for materials in the degrader loop.

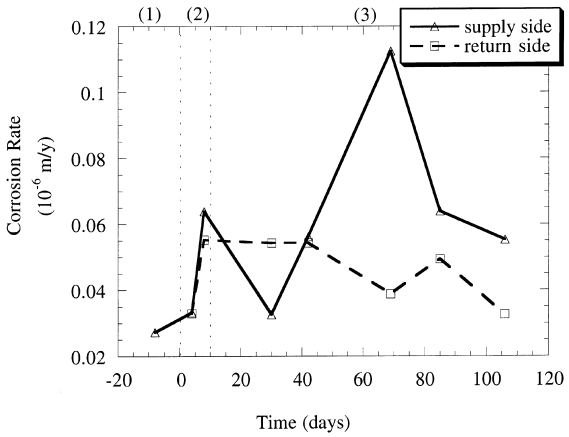

Fig. 15. Corrosion rates for 304L SS in the corrosion water loop as a function of irradiation time. The irradiation period has been divided into three separate categories as described in Figs. 2 and 9.

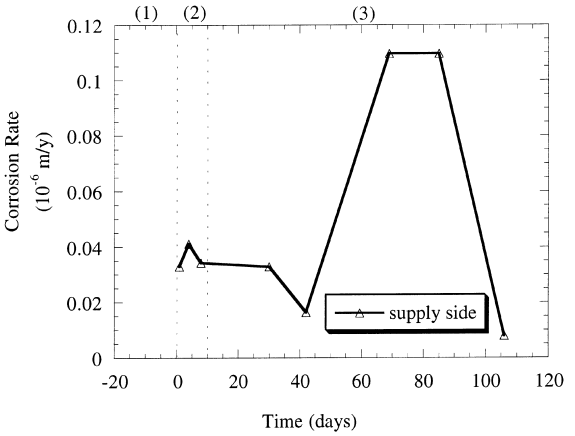

Fig. 16. Corrosion rates for Alloy 718 in the corrosion water loop as a function of irradiation time. The irradiation period has been divided into three separate categories as described in Figs. 2 and 9.

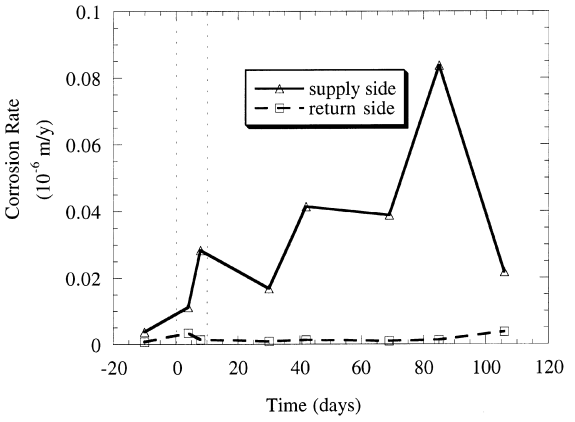

Fig. 17. Corrosion rates for Ta in the corrosion water loop as a function of irradiation time. The irradiation period has been divided into three separate categories as described in Figs. 2 and 9.

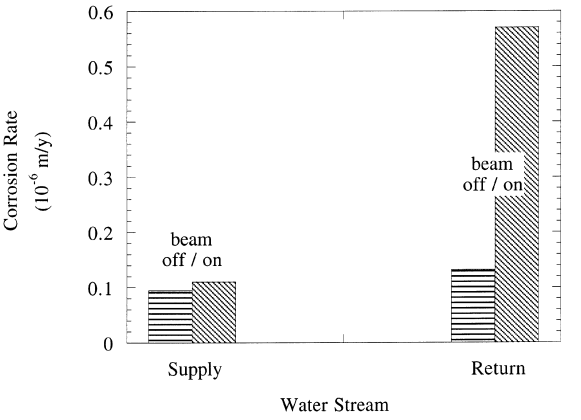

Fig. 18. Corrosion rates for Cu from the degrader loop. Data were taken on day 0 in Fig. 19 before and after the proton beam was turned on at 1.0 mA.

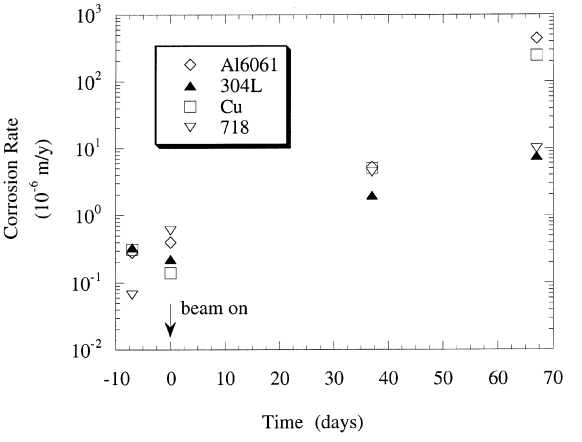

Fig. 19. Corrosion rate for Al6061, 304L SS, Cu, and Alloy 718 in the degrader loop (return side) as a function irradiation time. Negative time indicates the pre-irradiation period (beam off). Proton beam current was 1.0 mA throughout the irradiation period.

With the beam off, the corrosion rates for Cu in the return and supply side streams were approximately the same, 0.13 and 0.096 μm/yr respectively (Fig. 18). Upon turning the proton beam on to a current of 1.0 mA, the corrosion rate of the return side Cu sample increased to 0.57 μm/yr while the corrosion rate of the supply side Cu sample remained the same.

The long-term corrosion rates for Alloy 718, 304L SS, and Al6061 were considerably higher than those measured for these same materials in the corrosion loop (Fig. 19). For example, after 40 days of immersion (approximately 2×10^{26} p/m^2) the corrosion rates of Al6061 and 304L SS in the corrosion loop were approximately 0.55 and 0.054 μm/yr respectively. In comparison, the corrosion rates of Al6061 and 304L SS in the degrader loop after 40 days of immersion (approximately 4×10^{25} p/m^2) were approximately 5.6 and 1.9 μm/yr. These differences in corrosion rates between the systems are attributed to differences in water quality during irradiation. In comparison to the corrosion loop, water resistivity for the degrader loop (Fig. 20, return stream) decreased from its initial value of approximately 1×10^5 Ω cm to a final value of 1.7×10^3 Ω cm at the end of the irradiation period. This decrease was attributed to an increase in both radiolysis products (due to the higher proton fluence in the degrader loop) and corrosion products (due to the materials used to construct the degrader loop). In addition, water in

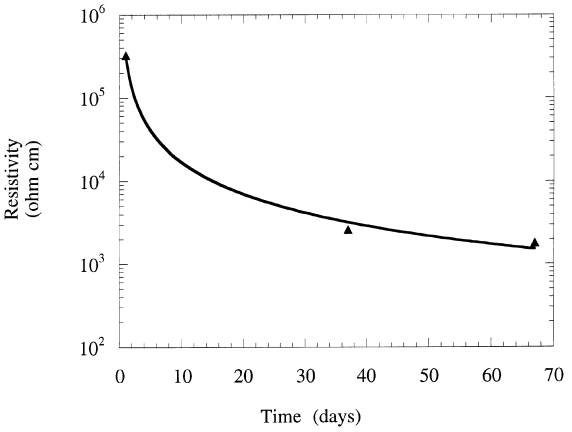

Fig. 20. Water resistivity from the degrader loop as a function of irradiation time (return stream only).

the degrader loop had a resonance time of approximately 16 s at the proton beam spot, thus for equivalent proton fluences in both loops, the concentration of radiolysis products is anticipated to be higher in the degrader loop as water in the corrosion loop manifold was not associated with a resonance time. Post-irradiation analysis of the degrader loop water system found that copious amounts of Cu^{++} (in the form of Cu/CuO) that had plated out on virtually all components. Copper precipitation was not an issue in the corrosion water loop system as it was entirely fabricated of 304 SS and contained no Cu corrosion samples. It has been recognized for quite some time that Cu/CuO precipitation increases cathodic reaction rates and thus metal corrosion [6]. Although this phenomenon occurs in nickel and iron base alloys, aluminum alloys are particularly sensitive to Cu precipitation which likely explains the relatively high rates of aluminum corrosion observed in the degrader loop (Fig. 19).

4. Conclusions

A method for measuring the real-time corrosion rates of materials in water irradiated by 800 MeV protons has been presented. The effects of water system fabrication materials, hydrogen water chemistry, and pre-cleaning of the water system on corrosion rate have been demonstrated to be dramatic. In the corrosion loop which was fabricated entirely of 304 SS, thoroughly cleaned before operation, and employed hydrogen water chemistry to mitigate the formation of radiolysis products, the corrosion rates for stainless steels, Alloy 718, and tantalum were extremely low, less than 0.12 μm/yr. For Al6061 and Al5052, the corrosion rates were slightly higher than the iron and nickel base alloys, of the order of 0.50–2.0 μm/yr. The corrosion rate of tungsten was found to be (relatively) high, between 5.0 and 30 μm/yr. In comparison, the corrosion rates of these materials in the degrader water loop which was fabricated from copper piping and stainless steel, was not cleaned prior to operation, and employed no HWC were 1–3 orders of magnitude higher.

These results were attributed to a change in water purity and a build-up of water radiolysis products within the closed loop systems. In the system with the lowest corrosion rates (corrosion loop) the water resistivity remained between approximately 8×10^4 and 3×10^4 Ω cm. The largest decrease in resistivity was observed when the proton beam was turned on. In comparison, during the same time period, the resistivity of degrader water loop fell from its initial value of approximately 1×10^5 to 2×10^3 Ω cm. ICP analysis, iodometric titration, and Gamma analysis of the water from the corrosion loop were consistent with resistivity measurements. ICP analysis of water samples found only trace amounts of Mg, Zn, Cu, and Ca, believed to come from the DI water as they were observed prior to turning the beam on and their concentration was independent of irradiation time. Iodometric titration of water samples found that the concentration of H_2O_2 in the water system at the end of the irradiation period was low, 0.34 mol/m^3. In comparison, post-irradiation analysis of the degrader loop water system found that copious amounts of Cu^{++} (in the form of Cu/CuO) had plated out on virtually all of the components.

In conclusion, the present investigation has demonstrated that the corrosion rates of materials in a spallation neutron cooling (downstream from the proton beam) can be mitigated by carefully controlling water purity, hydrogen water chemistry, and eliminating copper and copper alloyed components. The rates reported on here may reduced further by increasing the dissolved hydrogen concentration, adding on-line water purification, and regularly flushing the cooling water system.

Acknowledgements

All work in this project was performed by the University of California under the auspices of the US Department of Energy contract W-7405-ENG-36. The authors would like to thank Laurie Waters and the continued financial assistance of the APT project office; Luke Daemen for helpful discussions and peroxide analysis; Walt Sommer for helpful discussions; Stuart Maloy for help with water analysis and discussions; Richard Werbeck, Bob Brown, Eugene Zimmerman and the rest of the LANSCE-7 group for their engineering expertise in the fabrication of the corrosion insert; and Greg Chandler (SRS) who assisted with some of the experiments.

References

[1] T.K. Yeh, D.D. MacDonald, T.A. Motta, Nucl. Sci. Eng. 121 (1995) 468.
[2] H. Christensen, Nucl. Technol. 109 (1994) 373.
[3] J.L. Magee, A. Chatterjee, Kinetics of Nonhomogeneous Processes, in: G.R. Freeman (Ed.), Wiley, New York, 1987, p. 171.
[4] L.L. Daemen et al., Materials for Spallation Neutron Sources, in: M.S. Wechsler, L.K. Mansur, C.L. Snead, W.F. Sommer (Eds.), Orlando, FL, 10–12 February 1997, TMS, Warrendale, PA, 1998.
[5] W.G. Burns, P.B. Moore, Radiat. Eff. 30 (1976) 233.
[6] H. Kaesche, Metallic Corrosion, NACE, 1985.
[7] M.E. Indig, J.E. Weber, in: Corrosion/83, NACE, Houston, TX, paper no. 124, 1983.
[8] W.R. Kassen, R.P. Jones, J.L. Tollefson, in: Corrosion/92, NACE, Houston, TX, paper no. 112, 1992.
[9] M. Fox, in: Corrosion/83, NACE, Houston, TX, paper no. 123, 1983.
[10] C.C. Lin, R.L. Cowan, R.S. Pathania, in: Corrosion/93, NACE, Houston, TX, paper no. 619, 1993.
[11] L.G. Ljungberg, D. Cubicciotti, M. Trolle, in: Corrosion/85, NACE, Houston, TX, paper no. 100, 1985.
[12] M.J. Fox, A review of boiling water reactor chemistry: science, technology, and performance, Argonne National Laboratory for the US Nuclear Regulatory Commision NUREG/CR-5115 ANL-88-42, 1989.
[13] Y.J. Kim, in: Corrosion/96, NACE, Houston, TX, paper no. 102, 1996.
[14] Y.J. Kim, P.L. Andresen, T.M. Angeliu, in: Corrosion/96, NACE, Houston, paper no. 109, 1996.
[15] R.S. Glass, G.E. Overturf, R.A.V. Konynenburg, R.D. McCright, Corros. Sci. 26 (8) (1986) 577.
[16] Y.J. Kim, R.A. Oriani, Corrosion 43 (2) (1987) 92.
[17] A.V. Byalobzheskii, Radiation Corrosion, Keter, Jerusalem, Israel, 1970 (Russian translation).
[18] S. Fujimoto, T. Yamada, T. Shibata, J. Electrochem. Soc. 145 (1998) L79.
[19] Y.J. Kim, R.A. Oriani, Corrosion 43 (2) (1987) 85.
[20] G. Capobianco, G. Palma, G. Granozzi, A. Glisenti, Corros. Sci. 33 (5) (1992) 729.
[21] R.S. Lillard, D.P. Butt, Mater. Character., accepted.
[22] R.S. Lillard, D.P. Butt, J. Mater. 50 (12) (1998) 56.
[23] R.S. Lillard, D.L. Pile, D.P. Butt, J. Nucl. Mater., accepted.
[24] W.F. Sommer, APT materials safety experiments technical report, Los Alamos National Laboratory LAUR-93-2850, 1993.
[25] L.B. Kriksunov, D.D. MacDonald, P.J. Millet, J. Electrochem. Soc. 141 (11) (1994) 3002.
[26] I. Epelboin, C. Gabrielli, M. Keddam, H. Takenouti, in: F. Mansfeld, U. Bertocci (Eds.), Electrochemical Corrosion Testing, ASTM STP 727, ASTM, Philadelphia, 1981, p. 150.
[27] D.D. MacDonald, in: F. Mansfeld, U. Bertocci (Eds.), Electrochemical Corrosion Testing, ASTM STP 727, ASTM, Philadelphia, 1981, p. 110.
[28] J.O.M. Bockris, A.K.N. Ready, Modern Electrochemistry, vol. 2, Plenum, New York, 1973.
[29] F. Mansfeld, in: R. Baboian (Ed.), Electrochemical Techniques, NACE, Houston, 1986, p. 67.